INL/JOU-23-74697-Revision-0

Accelerated thermal property mapping of TRISO advanced nuclear fuel

March 2024

Michael J Moorehead, Zilong Hua, Kevin Daniel Vallejo, Boone Beausoleil, Amey Rajendra Khanolkar, Tyler Gerczak, Marat Khafizov, David H Hurley

Changing the World's Energy Future

Idaho National Laboratory

INL is a U.S. Department of Energy National Laboratory operated by Battelle Energy Alliance, LLC

INL/JOU-23-74697-Revision-0

Accelerated thermal property mapping of TRISO advanced nuclear fuel

Michael J Moorehead, Zilong Hua, Kevin Daniel Vallejo, Boone Beausoleil, Amey Rajendra Khanolkar, Tyler Gerczak, Marat Khafizov, David H Hurley

March 2024

Idaho National Laboratory
Idaho Falls, Idaho 83415

http://www.inl.gov

Prepared for the
U.S. Department of Energy
Under DOE Idaho Operations Office
Contract DE-AC07-05ID14517, DE-AC07-05ID14517

Accelerated Thermal Property Mapping of TRISO Advanced Nuclear Fuel

Authors:

Michael Moorehead[1]✉, Zilong Hua[1], Kevin Vallejo[1], Geoffrey Leonard Beausoleil II[1], Amey Khanolkar[1], Tyler Gerczak[2], Marat Khafizov[3], David Hurley[1]

Affiliations:

[1]: Idaho National Laboratory, 1955 N Fremont Ave, Idaho Falls, ID 83415

[2]: Oak Ridge National Laboratory, 5200, 1 Bethel Valley Rd, Oak Ridge, TN 37830

[3]: The Ohio State University, 281 W Lane Ave, Columbus, OH 43210

Keywords: TRISO, thermoreflectance, thermal diffusivity, thermal conductivity, nuclear energy

Highlights:

- The thermal properties of a single TRISO particle were mapped up to 1000 °C.
- Anisotropy and variation of thermal properties over multiple particles was studied.
- Microstructural causes for differences in TRISO thermal properties are provided.
- A simplified technique to rapidly map thermal properties has been developed.

Graphical Abstract:

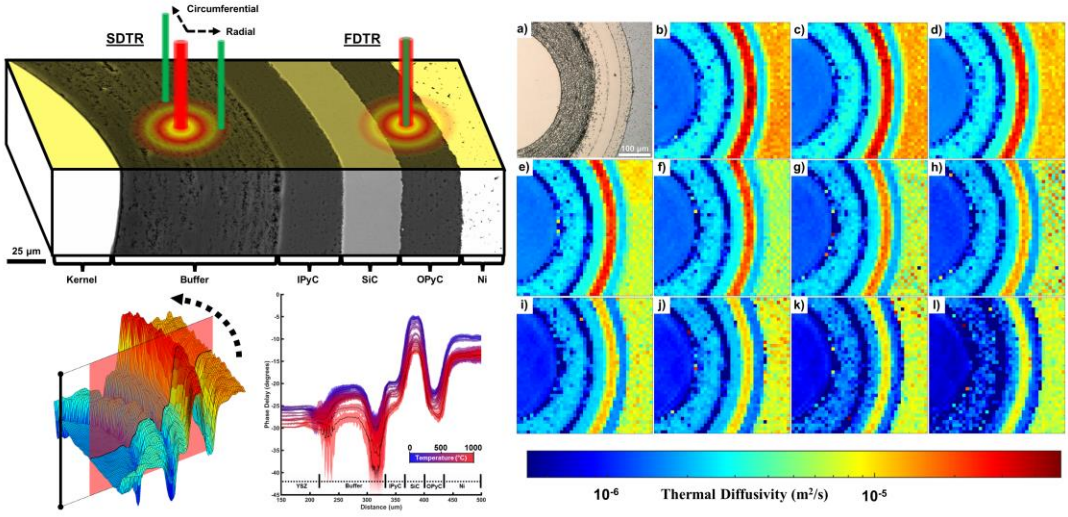

✉ 1955 N Fremont Ave, Idaho Falls, ID 83415| (480) 329-6188 | michael.moorehead@inl.gov

Abstract:

TRistructural ISOtropic (TRISO) fuel is a leading-edge nuclear fuel form representing a departure from the more traditional nuclear fuel forms utilized in the reactor fleet of today. Rather than a monolithic fuel pellet of uranium dioxide, integral fuel forms containing TRISO fuel are composed of thousands of microencapsulated uranium-bearing fuel kernels and individually coated with multiple layers of pyrolytic carbon and silicon carbide. These multilayered ceramic coatings serve as an environmental barrier to ensure radioactive and chemically reactive fission products are contained within the reactor fuel elements, but also participate in the transfer of heat generated in the nuclear fuel to the coolant – the primary purpose of a nuclear reactor. Since traditional thermal property measurement techniques, such as laser flash analysis, would be unable to resolve the thermal properties of the individual TRISO coating layers, a simplified frequency-domain thermoreflectance technique has been developed to rapidly map the thermal properties of TRISO particles. Using this technique, the thermal properties of TRISO particles have been mapped from room temperature up to 1000 °C to examine the spatial variation and temperature-dependency of the thermal properties within each layer. Additionally, spatial-domain thermoreflectance was used to examine the anisotropy of the thermal properties for each layer at different locations within a single TRISO particle, and across multiple TRISO particles to assess the intra- and inter-particle uniformity of thermal properties, respectively. To elucidate the underlying causes for the measured variations in thermal properties, scanning electron microscopy and Raman spectroscopy were used to examine variations in microstructure and chemical bonding within the different coating layers. Results from this work are then compared with previous examinations of TRISO fuel particles and microstructurally driven mechanisms for the variations in the measured thermal properties of the different carbonaceous layers are discussed.

1. Introduction and Motivation

Following the historic earthquake and resultant tsunami that precipitated the meltdowns at the Fukushima Daiichi Nuclear Power Plant in 2011, interest has grown in developing accident-tolerant nuclear fuels and deploying new advanced reactor technologies with enhanced safety features, alongside improved efficiencies and versatility [1]. TRistructural ISOtropic (TRISO) fuel is one such advanced nuclear fuel form that, while in development for decades prior, has gained new traction in recent years as the fuel form of choice for advanced reactor designs put forth by the United States Department of Defense (DoD) and Department of Energy (DOE) as well as the private sector [2]. Both mainstays and newcomers to the nuclear industry have put forward reactor designs which seek to employ TRISO fuel, including Westinghouse as well as X-energy, Kairos, Radiant, Ultra Safe Nuclear Corporation (USNC) and others. Unlike the monolithic UO_2 fuel utilized by nearly all operating nuclear reactors today, TRISO fuel consists of fuel dispersoids embedded in a matrix material. These dispersoids consist of a spherical fuel kernel, typically made of uranium oxide (UO_2), multiphase uranium oxide, uranium carbide (UCO) or uranium nitride (UN), surrounded by a porous carbon buffer layer and encased in a three-layer shell consisting of a silicon carbide (SiC) layer sandwiched between two pyrolytic carbon layers, the inner pyrolytic carbon (IPyC) layer and the outer pyrolytic carbon (OPyC) layer [3].

TRISO particles offer many benefits over traditional nuclear fuels. During reactor operation, the swelling of the fuel kernel and the generation of fission products are accommodated by the porous buffer layer, which provides space for fission products and fission gases to reside and can deform to accommodate geometric changes of the kernel while the three-layer shell provides structural integrity and serves as a barrier to prevent diffusion of the fission products out of the individual particle. By retaining the fission products within each individual TRISO particle, structural materials within the reactor are protected from the chemically aggressive medley of elements born out of fission that can react with and embrittle core components (e.g., fuel cladding). Moreover, given the small size of the TRISO particles (~800-μm-diameter spheres) versus that of convention UO_2 fuel pellets (~ 1-cm-by-1-cm cylinders), the mechanical failure of

a single TRISO particle releases a far smaller amount of fission products than the failure of a UO_2 pellet, thereby improving safety by introducing redundancy. From the perspective of reactor manufacturer or utility, another major benefit is the ability to achieve higher power densities and operating temperatures without raising the centerline temperature of the fuel above safe levels, which is enabled by embedding the TRISO particles in a thermally conductive matrix, typically made of graphite [3] or occasionally SiC [4] Such TRISO particle fuel forms can be used in current generation light-water reactors (LWR), primarily as an accident-tolerant fuel with larger safety margins given typical LWR coolant temperatures (<300 °C), or their high-temperature stability can be exploited further by advanced reactor concepts such as high-temperature gas reactors (HTGR), which have outlet temperatures above 700 °C and boast higher efficiencies as well as enable the practical utilization of nuclear reactors for process heat and hydrogen production.

The generation of heat within nuclear fuel materials is both the purpose of nuclear reactors and one of the challenges which limits the safety and efficiency of reactor systems. Specifically, heat generated within the fuel elements must be removed for the reactor to perform useful work, but also to ensure that the fuel elements retain a coolable geometry and that the maximum temperature of the fuel remains within design limits – else fission product release and microstructural evolution of the fuel can accelerate and lead to increased mechanical stresses and potential deleterious chemical interactions within the fuel and with structural materials elsewhere in the reactor [5]. Moreover, the thermal transport properties in reactor fuels evolve over time, typically degrading with increasing fuel burnup as more fission products are generated and more voids, bubbles, dislocations, and secondary phases are formed within both the fuel and core structural materials [6]. As such, understanding the thermal transport properties of nuclear fuel elements over a broad range of operating conditions is paramount, and equally so for multi-material fuel elements like TRISO particles. Typically, the thermal transport properties (e.g., thermal diffusivity) of bulk materials are measured using laser flash analysis (LFA), which involves machining a sample to have parallel faces, applying a laser (heat) pulse to one face of the sample, and measuring the time-dependent temperature rise on the opposing face. While LFA can be used to measure bulk and quasi-homogeneous materials, the small

length scales and architected nature of TRISO particles prevent the thermal properties of each individual layer from being resolved using LFA. Other techniques such as the guarded-comparative heat flow technique, wherein a rod of unknown thermal conductivity is flanked by two rods of known thermal conductivity which are collectively subjected to an applied steady-state heat flux to determine the properties of the unknown rod, have also been applied to graphitic TRISO compacts [7], however, such techniques can only be used to determine an *effective* thermal conductivity which averages over all of the layers of many particles as well as the matrix material. Such macroscopically averaged property measurements preclude the ability to resolve differences in the local thermal properties resulting from the microscopic heterogeneities (i.e., different TRISO layers), which can lead to inaccurate predictions of the fuel kernel temperatures and thus the fuel performance. To avoid this, previous efforts to study the thermal properties of TRISO coating layers have employed Raman-based techniques [8] or laser-based thermoreflectance techniques [9-11], which offer much finer spatial resolution. Unfortunately, there is substantial scatter in the reported thermal diffusivity and conductivity values in the literature, especially in the SiC TRISO layer, whose reported room temperature thermal conductivity varies from 4 W/m·K [8] to 168 W/m·K [9] and occasionally is omitted from the layers reported on [10]. Additionally, the anisotropy of the thermal properties within a given pyrolytic carbon layer, given as the ratio between the thermal diffusivity or conductivity in the circumferential versus the radial direction, has been reported in the literature to range from 1.01 to more than 40 depending on processing conditions [10, 11]. Unfortunately, most of the thermal property measurements in the literature are from studies which examine only a single TRISO particle, and often only a single measurement from each layer within one particle. Moreover, much of the work previously performed has studied TRISO particles of unknown pedigree or *pseudo* TRISO particles – particles which feature carbonaceous coatings, but either feature different processing conditions or different layer materials than TRISO particles under consideration and undergoing qualification for reactor applications. As such, between variations in the processing conditions and the compositions of the materials studied, combined with the limited number of measurements taken, it is difficult to determine the origin of the scatter in the thermal property data for the different TRISO particle layers.

In this work, the directional thermal transport properties of each TRISO layer were directly measured using two laser-based thermoreflectance techniques and compared across multiple particles of known pedigree. Results from these measurements have then been examined in concert with microstructural characterization and Raman spectroscopy to gain understanding into the anisotropy of thermal properties within individual TRISO particles as well as the consistency of thermal properties at different locations within a single TRISO particle and across multiple TRISO particles. Additionally, a methodology has been developed to map the thermal properties throughout the cross section of a TRISO fuel particle, without requiring a priori knowledge of the underlying material, which can be extended to more general use in the material science community especially for applications involving other architected materials and metamaterials.

2. Methods and Materials

Surrogate TRISO particles (lot: ZRX05-26T) were sourced from Oak Ridge National Laboratory. The ZRX05 series of TRISO particles were initially produced to serve as surrogate particles for the uranium oxycarbide (UCO) fuel particles used during the second Advanced Gas Reactor (AGR-2) fuel campaign but manufactured using laboratory-scale equipment using process conditions comparable to those used for the AGR-2 fuel particles [12]. The ZRX05-26T surrogate TRISO particles are composed of a spherical yttria-stabilized zirconia (YSZ) kernel, approximately 400 μm in diameter, which has been sequentially coated with a ~100-μm buffer layer, a ~40-μm IPyC layer, a ~35-μm SiC layer, and finally a 40-μm OPyC layer. The coatings were applied using a fluidized-bed chemical-vapor deposition (FB-CVD) process using C_2H_2 as the precursor for the buffer, C_2H_2 + C_3H_6 for the pyrolytic carbon layers, and methyltrichlorosilane (MTS) + Ar/H_2 in a 1:1 ratio as the precursor for SiC; the reactions for applying the buffer, IPyC, SiC, and OPyC coatings were carried out at approximately 1400 °C, 1290 °C, 1425 °C, and 1290 °C, respectively. The TRISO particles used in this study were examined in the as-synthesized state, without overcoating and subsequent compaction and high-temperature sintering as would be typical in the production of a traditional

graphitic TRISO fuel compact. More information on TRISO particle synthesis and the history of the fuel form can be found in [2].

To prepare the surrogate TRISO particles for sample preparation and characterization, the surrogate TRISO particles were embedded in a nickel (Ni) compact via electric field assisted sintering (EFAS) using a Thermal Technology DCS-5. During EFAS, powders are placed between two punches surrounded by a die. The die assembly is placed between two water-cooled rams which compress the powder while simultaneously a direct-current (DC) voltage is applied to heat the assembly and consolidate the material. Temperature is monitored via a pyrometer which is directed at a bore hole through ~90% of the die wall thickness, which enables measurement of the temperature near the loaded powder. To produce the TRISO-Ni compacts, a 12-mm-diameter, G535 graphite die set was used. To minimize the likelihood of cracking any TRISO layers during compaction, a disc of 125-μm-thick Ni shim stock was loaded into the die to distribute the pressure across the TRISO particles. 25 surrogate TRISO particles were then loaded into the die followed by 3 g of Ni powder (Alfa Aesar, 3-7 μm average particle size) to form the compact. During EFAS, the die set was quickly ramped to 1000 °C at 100 °C/min, to minimize any microstructural evolution of the TRISO layers, while simultaneously pressure was ramped slowly up to 25 MPa at 3 MPa/min rather than preloading, to minimize the risk of particle fracture. The sample was held at 1000 °C for 60 seconds for the temperature to equilibrate after which the pressure was reduced to 10 MPa at 15 MPa/min while temperature was dropped to 300 °C at 100 °C/min before the system was turned off. Owing to the loading procedure and the relatively small number of particles used, all of the TRISO particles lie in the same plane at the bottom of the Ni compact, aiding in sample preparation. After EFAS synthesis, the compact was carefully ground using 320-grit SiC papers to a depth of approximately 40% of the diameter of the TRISO particles, to minimize pullout of the surrogate fuel kernels, and was then polished with incrementally finer SiC papers ending at 1200-grit which was followed by 9-, 3-, and 1-μm diamond suspensions and finally 0.04-μm colloidal silica. Optical microscopy was performed using a Keyence VHX-6000 series digital microscope to produce a stitched image of the TRISO-Ni compact, shown in Figure 1. Raman spectra were

obtained using a Horiba LabRam HR 800 confocal Raman microscope, with a Coherent Verdi laser (532 nm) and an objective lens of 50× to study the vibrational modes of the carbon layers. Scanning electron microscopy (SEM) and energy-dispersive spectroscopy (EDS) were performed using an FEI Quanta 650 SEM to examine the porosity of the TRISO layers and any interdiffusion that may have occurred between the TRISO particles and the Ni matrix during EFAS synthesis. Images were then processed using the software, ImageJ, to threshold the images in order to extract pore size distributions.

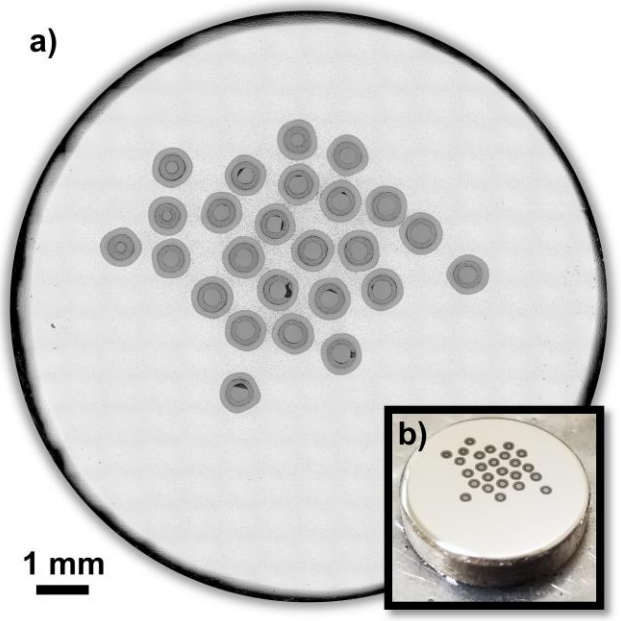

Figure 1: a) Stitched optical microscopy image and b) photograph of TRISO-Ni compact after EFAS synthesis and polishing.

To measure the thermal properties of the TRISO layers, two thermoreflectance-based techniques were employed: spatial-domain thermoreflectance (SDTR) [13-15] and frequency-domain thermoreflectance (FDTR) [16-19]. Both SDTR and FDTR employ a pump-probe setup, illustrated in Figure 2, wherein a 660-nm wavelength laser impinges on the surface of the sample with its amplitude modulated by a sinewave, using a function generator (Stanford Research System SD345), to locally heat the sample and produce a three-dimensional thermal wave within the material. In addition to the heating laser, a 532-nm wavelength laser is shined onto surface of the material with an unmodulated (i.e., constant) amplitude as a thermal wave probe. Using a lock-in amplifier (Stanford Research System SR860), the

thermal wave propagation is monitored by collecting the reflected probe laser beam, of which the periodic portion is a linear function of temperature, also known as the thermoreflectance effect. By comparing the phase delay of the induced thermal wave with respect to the applied heating, information about the thermal transport within the material can be gleamed – specifically the thermal diffusivity. To perform SDTR, the pump or probe laser spot is moved relative to one another, off of their initial coaxial alignment, which allows the in-plane thermal transport properties to be measured. The primary benefit of SDTR is that it enables the measurement of the thermal properties in an arbitrary direction across the surface of the sample which, through multiple measurements, allows the user to map the thermal properties along different vectors from a single point and assess any thermal anisotropy in the underlying material. Unfortunately, SDTR requires a larger sampling area, typically spanning ~10 – 20 μm in one dimension, (since the lasers necessarily must be positioned apart from one another) which limits the spatial resolution of the technique. To compliment SDTR, FDTR can be employed, which typically keeps the pump and probe beams coaxial as they interrogate the sample, while the pump beam is stepped through multiple modulation frequencies and the phase delay at each frequency is measured. The phase delays as a function of modulation frequency can then be fit to a thermal-wave model to fit the out-of-plane thermal properties. The advantages to this technique are that it can be used to interrogate a smaller volume, by eliminating the need to displace the lasers relative to one another, and that it can be performed substantially faster than SDTR, at the cost of collecting information on thermal property anisotropy. This technique was first used to map thermal effusivity of composite materials by Hatori et al [20], wherein the heating laser spot size was purposefully adjusted to ~10 μm such that a one-dimensional (1D) thermal-wave model could be used with the thermal effusivity of substrate as the only unknown parameter; this treatment had the effect of reducing the influence of the laser spot size on the measurements, while improving the accuracy of the fitting process. In contrast, the work presented herein was performed using a full three-dimensional (3D) thermal-wave model enabling the use of smaller laser spot sizes (~3.3 μm and ~1.3 μm for FDTR and SDTR, respectively) and consideration of a comparatively smaller measurement domain, confined within each layer of a given TRISO particle.

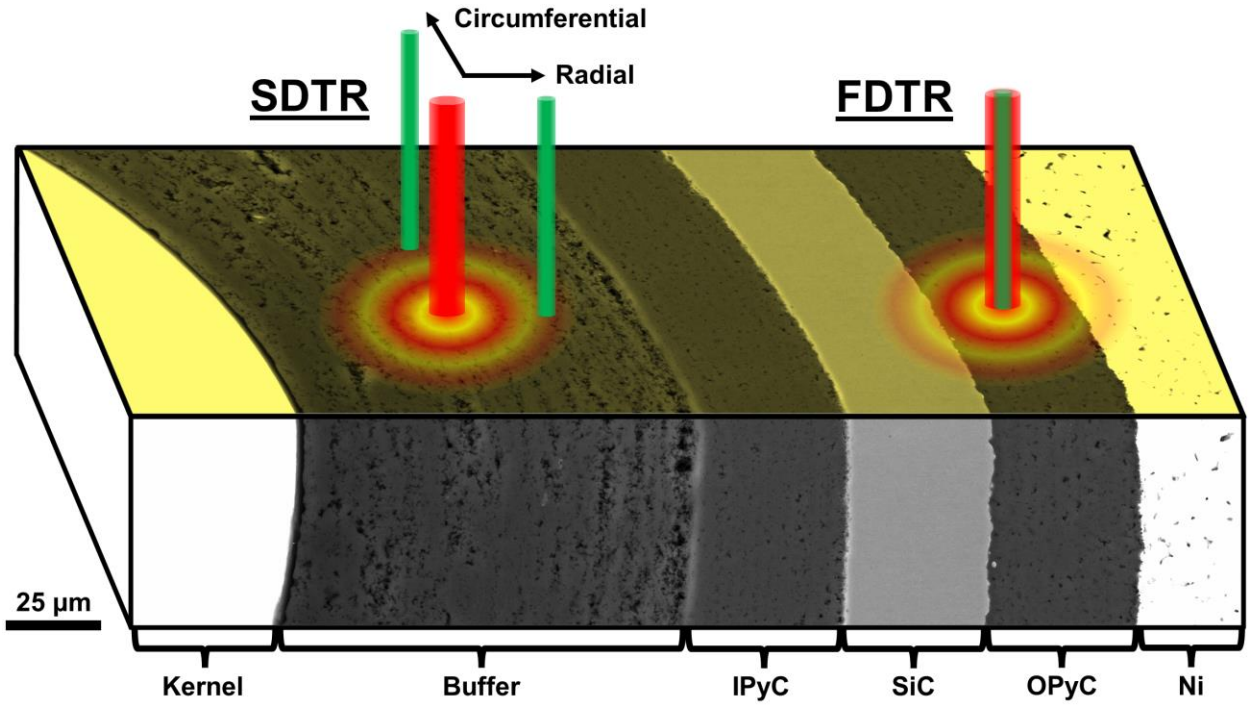

Figure 2: Illustration of spatial-domain thermoreflectance (SDTR) and frequency-domain thermoreflectance (FDTR) techniques employed to measure the thermal properties of the gold-coated TRISO-Ni compact.

To improve the signal and enable measurements of both thermal conductivities and diffusivities, a gold coating was deposited on top of the polished TRISO-Ni compact surface using a Quorum Q300T D Plus sputter coater. Gold was chosen as a coating material since it has a higher thermoreflectance coefficient with the 532-nm wavelength laser [21] and a higher melting point than aluminum - another coating material commonly used for thermoreflectance measurements using 800-nm wavelength lasers. Additionally, if the thickness, thermal conductivity, and heat capacity of the film are known, as well as the volumetric heat capacity of the underlying material, then for a fixed pump beam modulation frequency there is a unique thermal wave phase delay for a given thermal diffusivity value. Leveraging this, a lookup table was generated to convert measured phase delay to thermal diffusivity for the given experimental setup, enabling the rapid mapping of thermal diffusivity using only a single modulation frequency – reducing the FDTR thermal diffusivity measurement time to ~1 second per location. A sensitivity analysis was performed, following the procedure outlined by Hua et al. [22], to assess the optimal pump beam modulation frequency and gold film thickness to maximize the FDTR measurement sensitivity for thermal diffusivities near the

literature values of TRISO pyrolytic carbon, while simultaneously minimizing the measurement sensitivity to other process variables, such as laser spot size. From the sensitivity analysis, the optimal modulation frequency was found to be approximately 40 kHz and the optimal gold thickness was found to be approximately 50 nm, which was used as a target thickness for the sputtered film.

To determine the properties of the deposited gold film, which are necessary for generating the lookup table, a 2-mm-thick, transparent piece of borosilicate glass (BK7) was coated simultaneously with the TRISO-Ni compact. The thickness of the gold film was determined by measuring the attenuation of a 532-nm laser beam through the gold-coated BK7 and solving the Beer-Lambert law, with indices of refraction taken from literature [23], and was found to be 53 ± 3 nm. The thermal conductivity of the gold film was measured by performing SDTR measurements on the gold-coated BK7, the underlying substrate of which has known thermal properties [24]. The measured thermal conductivity of the gold film was found to be 195 ± 5 W/m·K, which can be used to solve for the thermal diffusivity, given the volumetric heat capacity of gold from literature [25], through (Equation 1:

$$D = \frac{k}{\rho C_P} \quad \text{(Equation 1)}$$

Here, D is the thermal diffusivity in m^2/s, k is the thermal conductivity in W/m·K, and ρC_P is the volumetric heat capacity in $J/m^3 \cdot K$. Since generating a lookup table to relate phase delay to thermal diffusivity requires a known volumetric heat capacity of the underlying material, of which there are many in the TRISO-Ni compact (e.g., YSZ, carbon, SiC, Ni), a single value must be chosen which can reasonably apply to all materials considered. Fortunately, the volumetric heat capacity of nearly all solid materials falls between ~$1\text{-}5 \cdot 10^6$ $J/m^3 \cdot K$, with most clustered around $3 \cdot 10^6$ $J/m^3 \cdot K$ at room temperature, and only gradually increases in magnitude as temperature increases [26]. Thus, $3 \cdot 10^6$ $J/m^3 \cdot K$ was selected as a baseline volumetric heat capacity to enable mapping the thermal properties using FDTR in a way that is agnostic to the underlying material. Thermal property mapping was performed under vacuum from room temperature up to 1000 °C, in 100-°C increments, using a Linkam TS1000 heating stage. The vacuum level for

measurements taken at 700 °C and below was maintained at ~$1 \cdot 10^{-5}$ torr, while the turbomolecular pump was throttled and the heating stage was backfilled with argon to produce vacuum levels of ~$1 \cdot 10^{-4}$ torr, ~$1 \cdot 10^{-3}$ torr, and ~$1 \cdot 10^{-2}$ torr at 800 °C, 900 °C, and 1000 °C, respectively, to minimize sublimation of the gold film at high temperatures due to its elevated vapor pressure [27].

Additionally, prior to applying the gold coating and performing thermal property measurements, the bonding structure of each layer was studied using Raman spectroscopy in a HORIBA LabRAM HR800 system. The laser used was a Coherent Verdi laser with a wavelength of 532 nm which was focused using a 50x microscope objective lens.

3. Results

3.1 Microstructural Characterization

To contextualize results from the thermal property measurements, the microstructures of the surrogate TRISO particles in the TRISO-Ni compact were first examined using SEM and EDS, shown in Figure 3. From the SEM imaging, Z-contrast using a backscattered-electron detector clearly reveals the different coating layers of a representative TRISO particle. Chemical mapping via EDS confirms both the composition of individual TRISO components and reveals a sharp interface between the OPyC of the TRISO particle and the Ni matrix, eliminating concerns of possible interdiffusion and chemical interaction of the TRISO particles and the Ni matrix during the EFAS process which could potentially affect other property measurements.

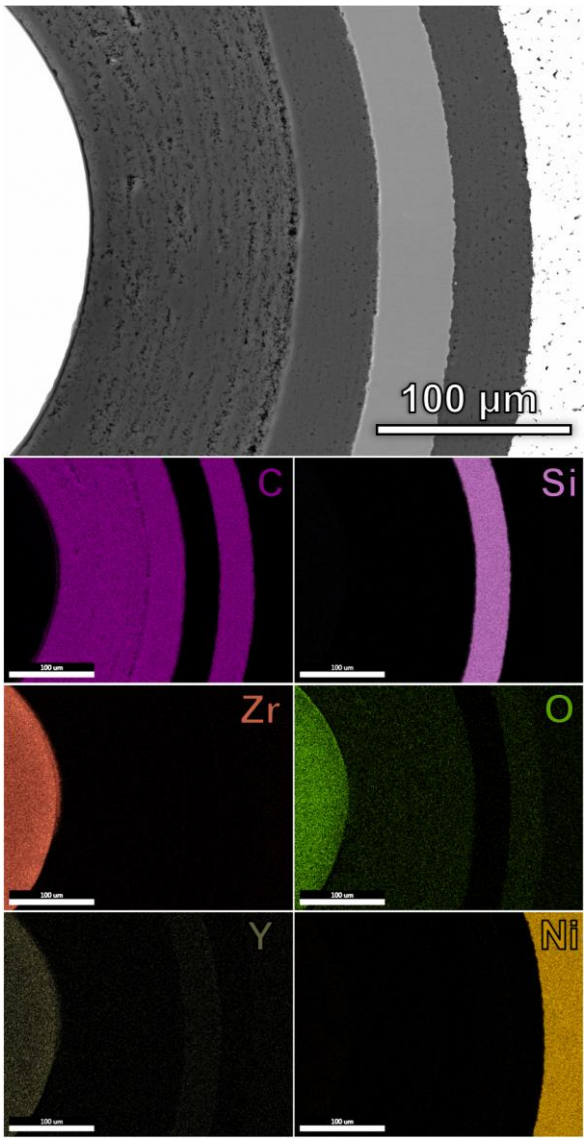

Figure 3: Backscattered-electron SEM and EDS chemical mapping of surrogate TRISO particle mounted in nickel via EFAS.

To further quantify the pore size distributions in each layer of the TRISO particles, SEM images of each layer were thresholded and segmented using ImageJ, with the size of each pore determined and binned using the average Feret diameter. The results from the porosity analysis are shown in Figure 4. After striking any pores identified from only a single pixel, to avoid tallying false positives at the resolution limit of the image, over 5,000 pores were analyzed, the results of which are given in Table 1. As designed, the buffer layer exhibits the highest porosity and the largest pore size of the coated layers, though the measured porosity (8.61%) is much lower than the design target (50% density) [2]. However,

the buffer layer porosity reported herein is comparable to recent work on surrogate particles from the same lot (ZRX05-26T) [28], where the authors found the porosity in the buffer to be 10.8% when using an intensity-based image segmentation technique and noted that this is likely an undercount compared to using deep learning model (19.3%), due to the challenges of image segmentation near the boundaries of pores where the contrast varies smoothly. It should be noted, that the typical TRISO buffer layer densities are nearly 50% of the theoretical density of graphite, which, given the comparatively low level of porosity measured in this study and others, implies the existence of pervasive nanopores and other nano-scale defects which are below the resolution of common microscopy techniques (e.g., optical, SEM) [28]. The measured pore size distributions in the carbonaceous layers (i.e., buffer, IPyC, and OPyC) each follow an exponential distribution, where the rate parameters for distributions are λ_{buffer}=1.35 μm^{-1}, λ_{IPyC} = 2.17 μm^{-1}, and λ_{OPyC} = 1.67 μm^{-1}, while the SiC layer had too few pores (four in sum) to meaningfully fit. The rate parameters for each layer indicate that the buffer layer has the broadest spread of pore sizes while the IPyC has the tightest spread, with the OPyC falling in between.

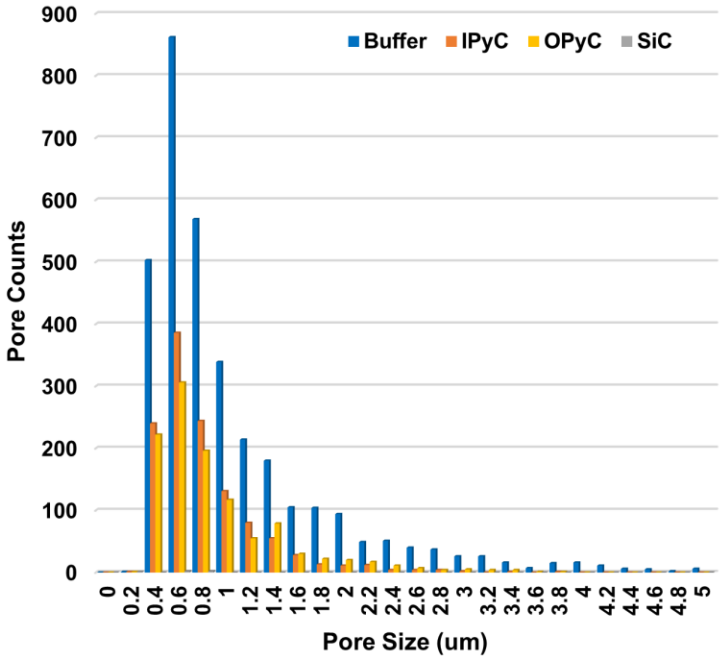

Figure 4: Pores size distributions for each of the TRISO layers as determined from SEM imaging. Pores identified occupying only a single pixel in the images were struck from the data set to avoid false positives.

Table 1. TRISO particle porosity measurement results.

	Buffer	IPyC	SiC	OPyC
Average Pore Size (µm)	1.02 ± 0.96	0.70 ± 0.46	0.60 ± 0.25	0.79 ± 0.56
Porosity (%)	8.61	5.35	<0.02	5.91
Exponential Distribution Rate Parameter (μm^{-1})	1.35	2.17	N/A	1.67

3.2 Thermal Property Characterization

3.2.1 Thermal Property Anisotropy and Homogeneity

To examine the homogeneity of thermal properties within each TRISO layer and the uniformity of properties between TRISO particles, three TRISO particles were divided into quadrants where two SDTR measurements were performed within each layer, in both the radial and circumferential directions, for a total of 96 measurements. Each SDTR measurement includes phase delay vs. laser displacement distance data collected at pump laser frequencies of 10 kHz, 20 kHz, 50 kHz, and 100 kHz which are fit to a heat diffusion model to determine thermal property values [22, 24], including thermal diffusivity, thermal conductivity, and volumetric heat capacity, shown in Figure 5. This set of frequencies was selected to ensure the thermal-wave penetration depth (i.e., the interaction volume) was localized within the measured layer and not substantially influenced by the adjacent dissimilar materials. Similar to the approach used by Hurley et al. [24], the 100 kHz phase delay (which is most sensitive to changes in thermal diffusivity) was kept to ensure the measurement sensitivity to thermal conductivity, while the remaining curves were displaced to have 0° phase delay at zero spatial offset to remove unnecessary fitting parameters. The room-temperature thermal properties calculated using SDTR measurements from each TRISO layer for three of the measured particles are given in Table 2.

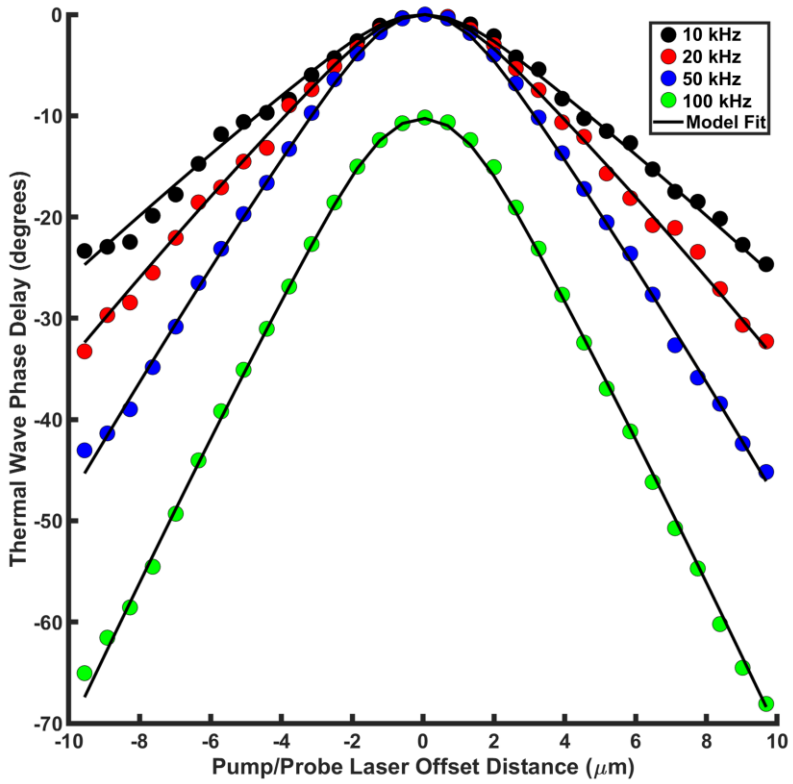

Figure 5: Example of spatial-domain thermal wave phase profiles collected during each SDTR measurement. Example shows data taken from the IPyC layer in the radial direction of a surrogate TRISO particle. Note that the 10 kHz, 20 kHz, and 50 kHz curves have been artificially displaced to have 0° phase delay with zero spatial offset to reduce the fitting parameters.

Table 2. Summary of results from SDTR measurements across multiple TRISO particles taken at room temperature, including the thermal diffusivity in the radial direction (D_R), thermal diffusivity in the circumferential direction (D_C), thermal conductivity in the radial direction (k_R), thermal conductivity in the circumferential direction (k_C), and the volumetric heat capacity (ρC_P). Uncertainties reported are based on the standard deviation of four measurements taken from different locations within a given particle and given layer under the same experimental conditions.

		Particle 1	**Particle 2**	**Particle 3**	**All Particles**
Buffer	D_R (m^2/s)	$(5.53 \pm 0.80)\cdot10^{-6}$	$(5.07 \pm 0.66)\cdot10^{-6}$	$(5.13 \pm 0.18)\cdot10^{-6}$	$(5.24 \pm 0.64)\cdot10^{-6}$
	D_C (m^2/s)	$(5.67 \pm 0.84)\cdot10^{-6}$	$(5.17 \pm 0.61)\cdot10^{-6}$	$(5.75 \pm 0.38)\cdot10^{-6}$	$(5.53 \pm 0.69)\cdot10^{-6}$
	k_R (W/m·K)	5.76 ± 0.37	5.64 ± 0.32	5.60 ± 0.64	5.67 ± 0.47
	k_C (W/m·K)	5.80 ± 0.45	5.21 ± 0.54	6.34 ± 0.21	5.78 ± 0.63
	ρC_P ($J/m^3\cdot K$)	$(1.06 \pm 0.19)\cdot10^{6}$	$(1.07 \pm 0.12)\cdot10^{6}$	$(1.10 \pm 0.12)\cdot10^{6}$	$(1.08 \pm 0.15)\cdot10^{6}$
IPyC	D_R (m^2/s)	$(4.34 \pm 0.73)\cdot10^{-6}$	$(4.06 \pm 0.35)\cdot10^{-6}$	$(4.45 \pm 0.46)\cdot10^{-6}$	$(4.28 \pm 0.56)\cdot10^{-6}$
	D_C (m^2/s)	$(4.52 \pm 1.00)\cdot10^{-6}$	$(4.04 \pm 0.85)\cdot10^{-6}$	$(4.60 \pm 0.90)\cdot10^{-6}$	$(4.39 \pm 0.95)\cdot10^{-6}$
	k_R (W/m·K)	6.33 ± 0.81	5.34 ± 0.38	6.38 ± 0.35	6.02 ± 0.74
	k_C (W/m·K)	5.88 ± 1.14	5.36 ± 1.66	5.92 ± 1.40	5.72 ± 1.44
	ρC_P ($J/m^3\cdot K$)	$(1.40 \pm 0.17)\cdot10^{6}$	$(1.32 \pm 0.17)\cdot10^{6}$	$(1.37 \pm 0.14)\cdot10^{6}$	$(1.36 \pm 0.16)\cdot10^{6}$
SiC	D_R (m^2/s)	$(10.06 \pm 2.67)\cdot10^{-6}$	$(12.07 \pm 1.24)\cdot10^{-6}$	$(11.53 \pm 4.51)\cdot10^{-6}$	$(11.14 \pm 3.34)\cdot10^{-6}$
	D_C (m^2/s)	$(9.64 \pm 1.16)\cdot10^{-6}$	$(10.04 \pm 0.73)\cdot10^{-6}$	$(7.70 \pm 1.06)\cdot10^{-6}$	$(9.04 \pm 1.45)\cdot10^{-6}$
	k_R (W/m·K)	34.63 ± 4.85	42.15 ± 3.61	36.84 ± 5.28	37.49 ± 5.59

	k_C (W/m·K)	40.88 ± 9.94	33.59 ± 4.38	30.74 ± 5.82	35.20 ± 8.55
	ρC_P (J/m^3·K)	(4.07 ± 1.49)·10^6	(3.43 ± 0.40)·10^6	(3.89 ± 1.36)·10^6	(3.83 ± 1.26)·10^6
OPyC	D_R (m^2/s)	(3.09 ± 0.38)·10^{-6}	(3.10 ± 0.73)·10^{-6}	(2.89 ± 0.19)·10^{-6}	(3.03 ± 0.50)·10^{-6}
	D_C (m^2/s)	(2.72 ± 0.32)·10^{-6}	(2.42 ± 0.32)·10^{-6}	(2.54 ± 0.26)·10^{-6}	(2.56 ± 0.33)·10^{-6}
	k_R (W/m·K)	3.92 ± 0.49	3.94 ± 0.64	3.51 ± 0.15	3.79 ± 0.51
	k_C (W/m·K)	3.30 ± 0.32	3.28 ± 0.71	3.30 ± 0.49	3.29 ± 0.53
	ρC_P (J/m^3·K)	(1.25 ± 0.10)·10^6	(1.33 ± 0.18)·10^6	(1.26 ± 0.10)·10^6	(1.28 ± 0.14)·10^6

Comparing measurements across multiple particles, none of the average property values measured for a given particle fell outside the 95% confidence interval of the entire population of values measured for a given property. Said in other words: for an α=0.05, the null hypothesis (that all of the particles are equivalent) cannot be rejected for any property in any particle, suggesting none of the differences in properties measured between the particles are statistically significant. This provides confidence in the uniformity of the TRISO manufacturing process and supports the usage of a single one of these TRISO particles to represent the population as a whole during the high-temperature thermal property mapping using FDTR. Thermal property values calculated for the carbonaceous layers from this collection of SDTR measurements are in good agreement with values reported in other thermal-reflectance-based studies [9, 29], though fall below values reported in Raman-based work [8]; thermal property values calculated for the SiC layer fall near the average of the values reported elsewhere in literature, however, the scatter of literature values is substantial and spans multiple orders of magnitude [8, 9, 29].While difference between particles were not found to be significant, some differences between the carbonaceous layers within a single particle were significant – namely the thermal diffusivities and conductivities of the OPyC. Despite being deposited under the exact same conditions as the IPyC layer, the thermal diffusivities and conductivities of the OPyC are all approximately 40% lower than their IPyC counterparts. Possible explanations for this have been provided in the literature, including annealing of the underlying layers during the SiC layer deposition, which may affect the dehydrogenation [30] and amorphous phase fraction of the deposited pyrolytic carbon [29], as well as differences in the residual stresses and texture of the deposited layers due to differences in cooling rates and the curvature of the layers at the different deposition radii, though this is usually thought

to be minimal [31-33]. Still, a mechanistic explanation cannot be provided from the thermal property measurements alone.

One of the main attractions to using SDTR is the ability to gleam direction-dependent thermal property information [22, 24, 34], especially given the wide range of thermal anisotropies reported for pyrolytic carbon coatings. Interestingly, in this study, none of the measured thermal diffusivities/conductivities measured in the radial direction were different enough from their counterparts in the circumferential direction for the difference to be statistically significant. Indeed, pyrolytic carbon deposition processing parameters are known to greatly affect the degree of anisotropy in the applied coatings, typically measured using optical reflectivity measurements [35, 36], and the evolution of the TRISO manufacturing process has strived to eliminate anisotropy in the properties of the coating materials. However, while thermal anisotropy has often been *inferred* from microstructural anisotropy in TRISO particles, the SDTR results presented herein demonstrate directly that the thermal properties of the individual layers are not anisotropic in any way that is statistically significant.

3.2.2 High-Temperature Thermal Property Mapping

Since TRISO fuel is being developed for next-generation nuclear reactor designs, it is important to understand how the thermal properties of the fuel vary as a function of temperature. To shed light on this, a series of FDTR measurements were conducted on the cross section of a single TRISO particle. Using a single modulation frequency (40 kHz) for the pump beam, the phase delay of the induced thermal wave at a given location was measured over a 1.5-second dwell time and correlated to a thermal diffusivity before moving to the next location; by repositioning the stage after every measurement following a raster pattern, the thermal diffusivity can be effectively mapped. A thermal diffusivity map was generated for the measured TRISO particle at room temperature and at 100-°C increments up to 1000 °C, as shown in Figure 6, with each map taking approximately 45 minutes to produce.

From the thermal diffusivity maps in Figure 6, the components of the TRISO particle are readily discernable based alone on the differences in their thermal properties. Here, the SiC layer stands out with the highest thermal diffusivities, measuring in excess of $5 \cdot 10^{-5}$ m^2/s at room temperature for some locations. The next highest room temperature thermal diffusivities, while not of primary interest to this study, were found in the Ni region, which were measured to be ~$1.5 \cdot 10^{-5}$ m^2/s to $2.0 \cdot 10^{-5}$ m^2/s which agrees well with values from literature [37]. Amongst the carbonaceous layers, the OPyC appears to have the lowest thermal diffusivity, ranging from ~2-$3 \cdot 10^{-6}$ m^2/s, while the buffer and the IPyC regions have similar thermal diffusivities, in the range of 3–$4 \cdot 10^{-6}$ m^2/s which all are within close agreement with the SDTR results. Finally, the YSZ fuel kernel simulant has the lowest thermal diffusivity ranging between ~1–$2 \cdot 10^{-6}$ m^2/s, which also agrees well with literature [38]. On either side of the buffer layer, a substantial drop in the measured thermal diffusivity is seen where the buffer has become detached from the YSZ and IPyC layers, leading to poor signal quality resulting in dead pixels which are reported as a thermal diffusivity of 0 m^2/s. In addition to enabling the rapid identification of the components within the TRISO particle based on differences in their thermal properties alone, the FDTR thermal diffusivity mapping also provides a qualitative assessment of the homogeneity within each layer. For example, the IPyC, OPyC, and YSZ appear relatively homogeneous in their thermal properties, while there is far more variation in the buffer layer likely resulting from the increase in overall porosity and the size of the pores which are on a similar order of magnitude as the laser spot size. While the SiC layer was found to have very little porosity from the SEM characterization, there is noticeable scatter in the data, likely owing to the reduced FDTR measurement sensitivity for materials with high thermal diffusivities when measuring with a modulation frequency of 40 kHz.

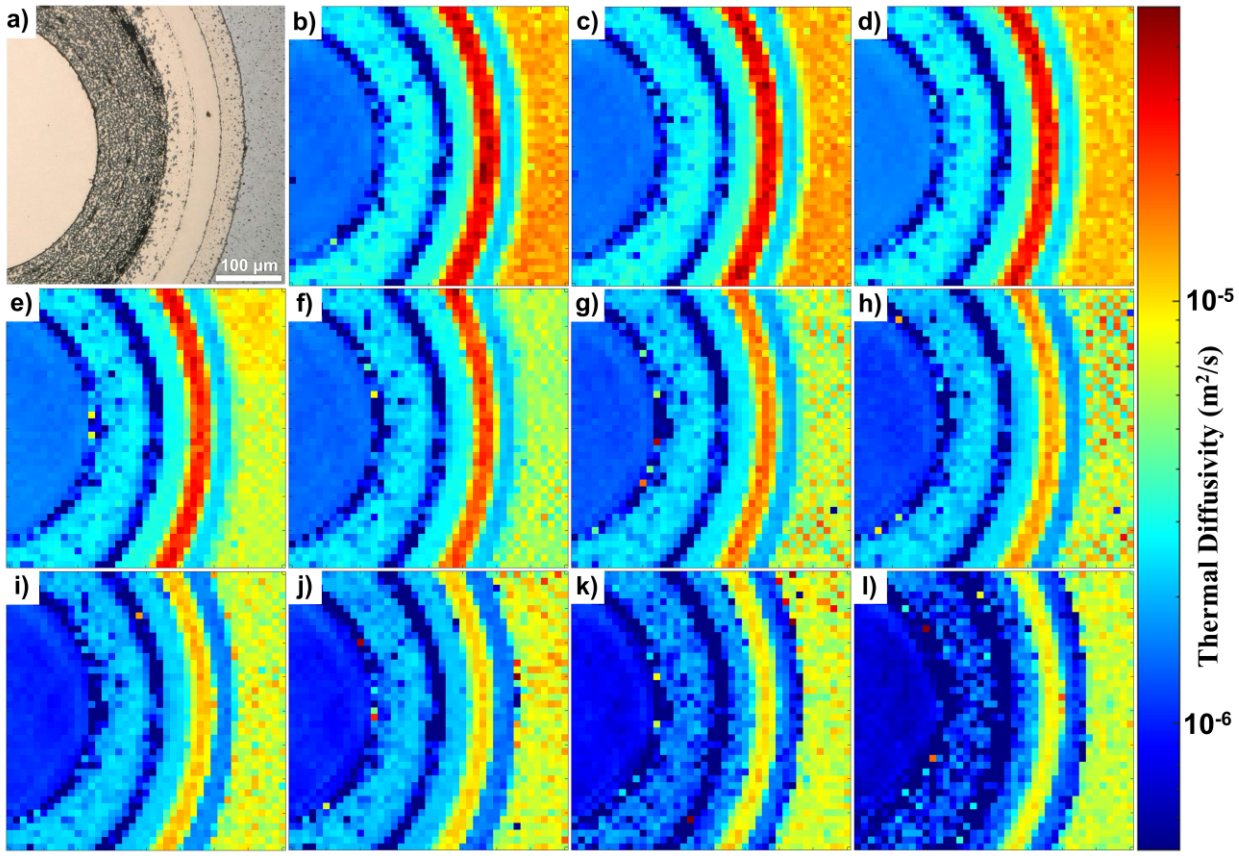

Figure 6: Thermal diffusivity mapping of TRISO particle embedded in Ni. a) optical image of TRISO particle after heating to 1000 °C in addition to thermal diffusivity maps generated at b) room temperature, c) 100 °C, d) 200 °C, e) 300 °C, f) 400 °C, g) 500 °C, h) 600 °C, i) 700 °C, j) 800 °C, k) 900 °C, and l) 1000 °C.

Upon heating the TRISO particles in the Ni compact, the thermal diffusivities of each TRISO component decrease monotonically with temperature, with the SiC experiencing the most dramatic decrease (from $>5 \cdot 10^{-5}$ m^2/s to $\sim 1 \cdot 10^{-5}$ m^2/s) over the measurement range of room temperature up to 1000 °C. Across all of the measurement temperature, the general ranking of the thermal diffusivities among the carbonaceous layers remains consistent, with the IPyC generally remaining the fastest (closely followed by the buffer) and the OPyC remaining the slowest. Above 800 °C, there is a substantial increase in the scatter of the data for the buffer region and to a lesser extent the IPyC region. It is posited that this increase in noise is caused by the restructuring and agglomeration of the gold film at elevated temperatures, which has been demonstrated to accelerate greatly over the 800–1000 °C temperature range [39], and appears to be facilitated by the increased porosity and surface roughness of the buffer region and the gap between the buffer and the IPyC, as evidenced by optical microscopy of the compact after heating to 1000 °C, shown in

Figure 6a. Additionally, though not a concern for the measurement of TRISO particles, in the post-measurement optical microscopy the gold film is shown to have completely disappeared from the Ni region, likely having diffused into the Ni at elevated temperatures given their mutual solubility and the relatively rapid diffusion of gold into Ni at these temperatures [40].

While the FDTR mapping methodology presented herein allows for the thermal diffusivities of multi-material structured to be rapidly mapped without need of defining the domains of different materials, assumptions baked into the generation of the lookup table, namely the assumption of a universal volumetric heat capacity ($3 \cdot 10^6$ J/m^3·K) for all materials at all temperatures, limit the quantitative accuracy of the technique. However, if the domains of the underlying materials are known – as well as the volumetric heat capacities of those materials at the measurement temperature – the phase delay data can be reprocessed to produce more accurate thermal diffusivity and conductivity values. To avoid needing to define the material properties of each individual pixel of the thermal diffusivity maps, the rotational symmetry of the TRISO particles can be exploited by performing a polar integral of the phase delay data about the center of the particle to collapse the two-dimensional map into a one-dimensional line scan in the radial direction, shown in Figure 7. From the one-dimensional line scans, individual regions can be given material assignments based on the known dimensions of each component of the surrogate TRISO particles. Here, the step change in the thermal wave phase delay can be seen at each material interface. Additionally, large uncertainties at the buffer interfaces are visible with the greatest uncertainties occurring at the poorly adhered IPyC/buffer interface which can be seen to increase as a function of temperature as the gold film restructures and wets the porous buffer region.

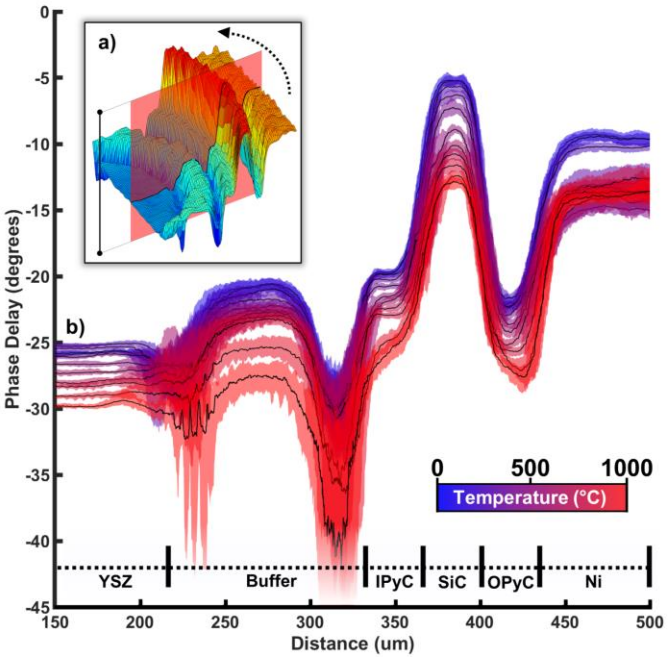

Figure 7: a) Schema for polar integration of the phase delay data from a two-dimensional FDTR map and b) the resultant one-dimensional line scans for each measurement temperature. Black lines indicate the average phase delay for a given radial position with the shaded color regions representing the bounds between the minimum and maximum values for a given radial position at a given temperature.

From the collapsed one-dimensional scans and the material assignments in Figure 7, the phase delay data can be refit with known heat capacity values from literature for each material to more accurately calculate the thermal diffusivities and conductivities. Measurements taken near the interface of two dissimilar materials (which would violate the semi-infinite boundary condition used in the thermal wave model) are omitted by only including phase delay data from the central "plateau" region within each layer visible in Figure 7; from the remaining valid data points, the thermal diffusivity and thermal conductivity of each material are calculated at each measurement temperature and are summarized in Figure 8. Here, the rapid decrease in thermal transport for SiC observed from the FDTR can be described more quantitatively as dropping from $6.57 \cdot 10^{-5}$ m^2/s to $1.04 \cdot 10^{-5}$ m^2/s when heated from room temperature. By comparison, over the same temperature range, the OPyC thermal diffusivity only decreases from $2.09 \cdot 10^{-6}$ m^2/s to $1.02 \cdot 10^{-6}$ m^2/s, with the buffer and IPyC layers following similar trends, save for the data points at 900 °C and 1000 °C for these regions which appear to be influenced by the degradation of the gold film. Another interesting feature of the thermal property temperature series is the sharp decrease and local minimum of

thermal diffusivity and thermal conductivity of the Ni region near 400 °C, above which the thermal diffusivity and thermal conductivity begin to increase. While artifacts in the data may be observed at elevated temperatures (>800 °C), at 400 °C, substantial reconstruction of the gold and/or diffusion into the Ni is not expected. Instead, this change in slope is the result of a magnetic phase transition which occurs at 358 °C, the Curie temperature, above which Ni transitions from ferromagnetic to paramagnetic and the slope of the thermal diffusivity and conductivity becomes positive with increasing temperature [41]. Though Ni was used in this work as high-temperature mounting media to facilitate the sample preparation of the TRISO particles and uniform heating during the high-temperature FDTR mapping and is otherwise inconsequential to the study of TRISO particles, the incidental observation of the magnetic phase transition illustrates the versatility and robustness of the simplified FDTR mapping technique in the examination of multi-material structures.

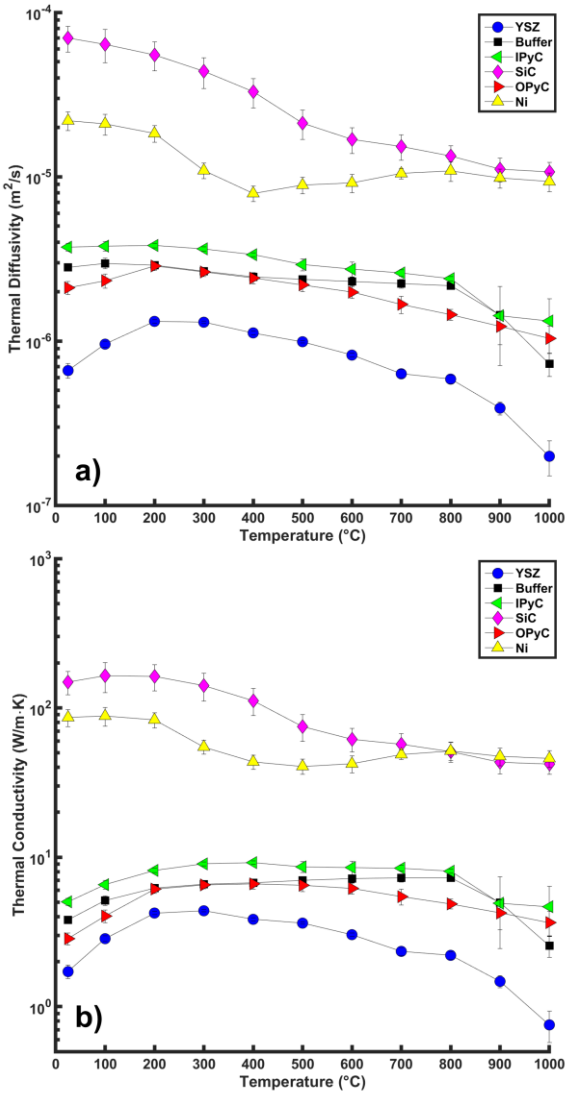

Figure 8: a) thermal diffusivity and b) thermal conductivity values for each material as a function of temperature produced by reprocessing the integrated one-dimensional phase delay data with assigned heat capacity values from literature. Error bars represent the standard deviation of the respective thermal property based on property values calculated from all phase-delay measurements for a given material at a given temperature within the TRISO particle.

3.3 Raman Analysis

The pyrolytic carbon layers surrounding the SiC have well-known structures that can be characterized by changes in the energy of a laser that stimulates vibrational modes in the graphene bonds [42]. Since pyrolytic carbon can be understood as a disordered stack of graphene sheets (i.e., turbostratic carbon), the degree of ordering in its structure, which has a major influence on its heat conduction properties, can be measured and understood from the peak intensity ratio between the two main modes A_{1g}

and E_{2g}. Understanding the microstructure of these various coating layers is important, as ultimately, efficient heat removal and the containment of fission products within the TRISO fuel depends on the structural stability of the coating layers.

In the buffer, IPyC, and OPyC layers, the A_{1g} and E_{2g} can be used to calculate the crystallite size according to the methodology proposed by Mallet-Ladeira et al. [43], where the ratio of peak intensities of these two modes is used as a parameter. Using this method, the crystallite sizes were calculated to be to be 4.16 nm for buffer, 4.68 nm for IPyC, and 5.01 nm for OPyC, following a trend of increasing size as the ratio of these peaks approaches unity, shown in Figure 9. Similarly, a series of laser powers were used to vary the heat supplied to the surface of the sample and monitor its thermal conductivity by tracking the peak-shift on the two modes studied, following [43]. Figure 10 shows a monotonic shift towards lower frequencies with higher laser power for each of the carbonaceous layers. Additionally, the spectra show clear second-order peaks located between 2700 – 2900 cm^{-1} which have been correlated to the degree of three-dimensional order along the stacking direction in pyrolytic carbon [44]. The change in intensity of these second-order peaks, as well as with the main A_{1g} and E_{2g} peaks, suggests the buffer layer has the greatest degree of graphitization while the IPyC and OPyC appear comparatively less graphitized.

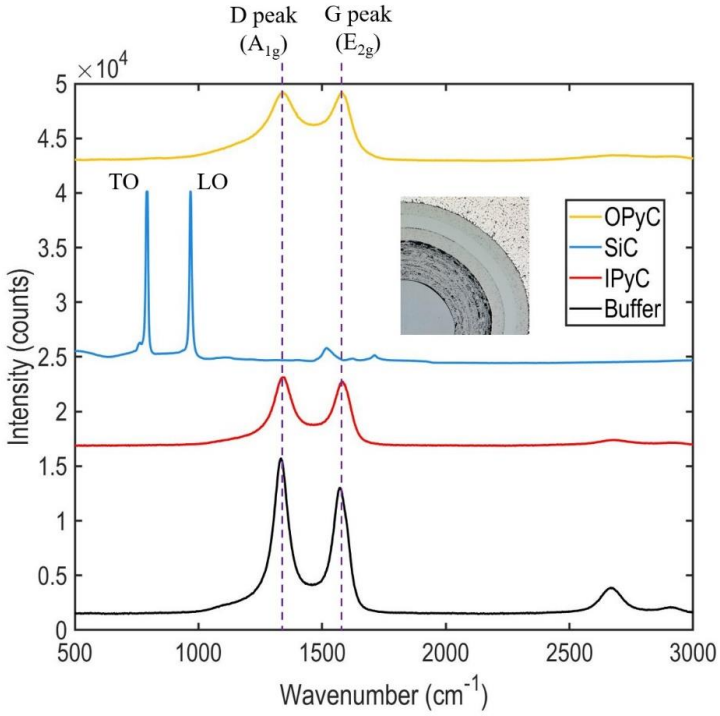

Figure 9: Raman spectra of the different layers of the TRISO particle (offset in the y-axis for comparison) measured with a laser power of 100 mW. Crystallite size is calculated from the intensity ratio of the A_{1g} and E_{2g} modes Raman peaks. Inset is a photograph of cross section of the TRISO particle examined.

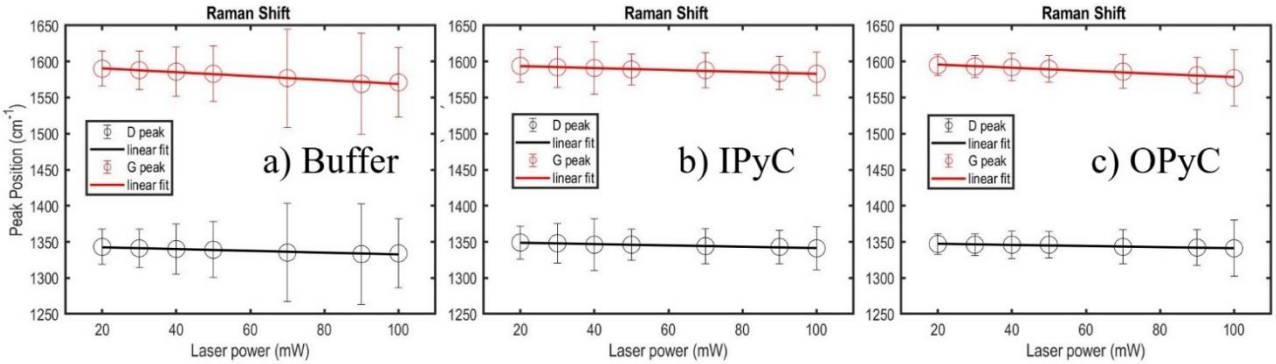

Figure 10: Laser power dependence of the D and G peaks in the a) buffer, b) IPyC, and c) OPyC layers of a TRISO particle.

4. Discussion

At first glance, it might seem strange that the IPyC layers were found to have thermal diffusivities ~50% greater than the OPyC layers, given their identical synthesis parameters and chemistry as well as their comparable porosity and comparable crystallite sizes, as determined by SEM and Raman analysis.

Indeed, the OPyC layer was actually found to have *larger* crystallites than the IPyC, which conventionally would be thought to increase thermal diffusivity by reducing phonon scattering from grain boundaries. Previous works have also observed substantial differences in IPyC and OPyC thermal diffusivities [8, 10, 29]. To reconcile this, it is necessary to consider the entire TRISO synthesis process. Following deposition of the IPyC layer at 1290 °C, the SiC layer is deposited at 1425 °C which has the effect of thermally annealing the underlying layers and reducing the phase fraction of amorphous/turbostratic carbon [45]. Since the OPyC is deposited at lower temperatures after the SiC layer, it would not be subject to the same thermal annealing and would be expected to have a larger phase fraction of amorphous/turbostratic carbon. Inspection of the Raman results in Figure 9 confirms that the OPyC contains a greater volume of amorphous/turbostratic carbon than the IPyC, as evidenced by the sharpness of the second-order located between 2700 – 2900 cm^{-1}, which are indicators of crystallinity. However, by this same token, the buffer layer is deposited at a higher temperature and exposed to more thermal annealing than the IPyC or OPyC layers and is the most graphitized based on the Raman observations, yet its thermal diffusivity/conductivity values are typically at or below those of the IPyC. Since its crystallite size is also comparable to the other pyrolytic carbon layers, the porosity is the only remaining microstructural feature that could explain the reduced thermal transport in the buffer layer. Thus, while more graphitized, the thermal transport in the buffer layer is dictated by porosity while the thermal transport in the IPyC and OPyC layers is dictated by the amorphous phase fraction. This means that the thermal diffusivities and conductivities of the pyrolytic carbon layers can be expected to improve with further annealing, as will occur during the compaction process whereby many TRISO particles are joined into a single fuel element by overcoating and sintering at 1800 °C, while the thermal properties of the buffer layer would not be expected to improve as markedly with additional annealing.

In general, the thermal diffusivity measurements taken using the simplified FDTR mapping technique are in excellent agreement with the comparatively slower and more rigorous SDTR measurements. However, the thermal diffusivity and conductivity of the buffer layer do appear greater when measured

using SDTR than FDTR, even after correcting the FDTR properties with heat capacity data from literature. Since the locations of the SDTR measurements within the buffer layer were chosen manually within each measurement quadrant, it is likely that cleaner locations (i.e., locations not directly adjacent to a major pore) were chosen to minimize noise and artifacts during data collection. By comparison, the FDTR measurements were collected using an entirely unbiased mapping process and averaged over a large measurement area, thus the FDTR measurements are thought to be more representative. In the cases of both the SDTR and FDTR measurements, however, the interrogation volume is relatively small compared to the buffer layer thickness, thus the thermal properties that are measured are representative of small volume elements within the buffer layer and may not ultimately be the same as an effective thermal diffusivity/conductivity through the entire buffer layer. For example, the circumferential bands of voids in the buffer layer may only represent a small fraction of the total measurement area in the FDTR mapping, only minorly affect the averaged properties for the buffer area, however, such a continuous band of voids would be expected to greatly affect the one-dimensional heat transfer in the radial direction through the entire buffer region and play an outsized role on the effective thermal diffusivity/conductivity through the entire layer. As such, it is important to holistically consider the microstructure of the material when interpreting localized thermal property measurements.

While initially developed and applied to the study of TRISO nuclear fuel elements, the simplified single-frequency FDTR mapping technique is inherently agnostic to the underlying material which means that it is broadly applicable to other areas of interest to the materials science community. Integrated circuits, thermoelectric stacks, composites, and other architected materials would all be well suited for thermal property mapping using the methodology presented herein, as would multiphase ceramics and metal alloys more generally. While not strictly necessary, the signal-to-noise ratio and the calculation of substrate thermal conductivity greatly benefit from the use of a thin film with a high thermoreflectance coefficient (e.g., aluminum, gold, platinum) of known thermal properties and thickness. However, as was observed with the measurements at 900 °C and 1000 °C, restructuring of the film and interaction of the film with the

substrate at elevated temperatures can have deleterious effects on the measurement accuracy – thus, the materials selection for the transducer layer governs the maximum temperature for data collection. Additionally, it should be noted that using only a single frequency to perform such thermal property measurements restricts the sensitivity range of the measurement technique. For example, in this study, a frequency of 40 kHz was selected to maximize the sensitivity for thermal diffusivities near those of pyrolytic carbon reported in literature. As a result, materials with thermal diffusivities much slower (e.g., YSZ) or faster (e.g., nickel and silicon carbide) than ~$5 \cdot 10^{-6}$ m^2/s produced greater uncertainties under these experimental conditions, as can be seen in Figure 8. Such uncertainties could be reduced by producing FDTR maps using multiple frequencies, however doing so would also increase the data acquisition time, thus recovering the traditional speed vs. accuracy tradeoff inherent to any measurement technique.

5. Concluding Remarks

TRISO particles are a paradigm-shifting nuclear fuel concept. Instead of using stacks of macroscopic uranium-bearing fuel pellets contained within stainless steel or zirconium tubes, a TRISO particle consists of a uranium-bearing fuel kernel ensconced in a multi-layer ceramic coating, that provides both mechanical integrity, fission-product retention, and a thermal transport pathway to harvest the heat produced by fission. By reducing the size of each uranium-bearing fuel element and individually encapsulating them, the severity of a single fuel element rupture is reduced, however, it remains critical to understand the properties and performance of the TRISO particle coatings. In this work, utilizing electric-field assisted sintering and multiple laser-based techniques, the following was achieved:

- From thermal property measurements collected via SDTR of each layer of multiple TRISO particles, it was found that differences in the thermal properties between TRISO particles are statistically insignificant, as are differences in the thermal properties in the radial and circumferential directions for a given layer.

- An improved methodology has been developed for a simplified version of FDTR, using a 3D thermal-wave model, a single modulation frequency, and a lookup table, which can rapidly map the thermal diffusivity of multi-material structures semi-quantitatively in a way that is agnostic to the domains of the underlying materials. If, however, some information is known about the underlying material (e.g., the volumetric heat capacity), this information can be added to the model to improve the accuracy afterwards.
- Applying the new FDTR mapping methodology to individual surrogate TRISO particles embedded in a Ni matrix (produced via EFAS), the thermal properties were mapped across all layers of the TRISO particles from room temperature up to 1000 °C. Owing to the rapid processing times and lower processing temperatures of EFAS, this allows the intrinsic thermal properties of the TRISO particles to be studied up at high temperatures absent any microstructural evolution which may occur during the compaction of many TRISO particles into macroscopic fuel elements, which often takes place at temperatures of ~1800 °C.
- From the Raman analysis, crystallite sizes were found to be comparable among all the carbonaceous layers, however, the buffer was found to be the most graphitized with the OPyC being the least graphitized and having the largest amorphous/turbostratic volume fraction, with the IPyC falling in between. Considering this finding, alongside the microstructural analysis, it was determined that the thermal transport in the IPyC and OPyC layers are limited by the amorphous/turbostratic phase fraction, while the thermal transport in the buffer is limited by the porosity.

Future work will include the analysis of surrogate TRISO particles in representative carbonaceous fuel compacts to assess the impact of the high-temperature compaction on the thermal properties of the TRISO particles in addition to studies including uranium-containing and neutron-irradiated TRISO particles.

Acknowledgements

This work was sponsored by the US Department of Energy through the advanced low enrichment uranium (aLEU) fuel project. This work was also supported by the Center for Thermal Energy Transport under Irradiation (TETI), an Energy Frontier Research Center funded by the US Department of Energy, Office of Science, Office of Basic Energy Sciences. Finally, the authors would like to thank Dr. John Hunn (Oak Ridge National Laboratory) and the DOE Advanced Gas Reactor Fuel Development and Qualification (AGR) program for synthesizing and providing the TRISO particles used in this study.

Data Availability

The raw/processed data required to reproduce these findings will be made available upon reasonable request.

References

[1] Accident Tolerant Fuel Concepts for Light Water Reactors, INTERNATIONAL ATOMIC ENERGY AGENCY, Vienna, 2016.
[2] P.A. Demkowicz, B. Liu, J.D. Hunn, Coated particle fuel: Historical perspectives and current progress, Journal of Nuclear Materials, 515 (2019) 434-450.
[3] J.A. Phillips, S.G. Nagley, E.L. Shaber, Fabrication of uranium oxycarbide kernels and compacts for HTR fuel, Nuclear Engineering and Design, 251 (2012) 261-281.
[4] K.A. Terrani, L.L. Snead, J.C. Gehin, Microencapsulated fuel technology for commercial light water and advanced reactor application, Journal of Nuclear Materials, 427 (2012) 209-224.
[5] W.J. Carmack, Temperature and Burnup Correlated FCCI in U-10Zr Metallic Fuel, in, United States, 2012.
[6] D.H. Hurley, A. El-Azab, M.S. Bryan, M.W.D. Cooper, C.A. Dennett, K. Gofryk, L. He, M. Khafizov, G.H. Lander, M.E. Manley, J.M. Mann, C.A. Marianetti, K. Rickert, F.A. Selim, M.R. Tonks, J.P. Wharry, Thermal Energy Transport in Oxide Nuclear Fuel, Chemical Reviews, 122 (2022) 3711-3762.
[7] C. Folsom, C. Xing, C. Jensen, H. Ban, D.W. Marshall, Experimental measurement and numerical modeling of the effective thermal conductivity of TRISO fuel compacts, Journal of Nuclear Materials, 458 (2015) 198-205.
[8] F. Cao, B. Liu, X. Wang, X. Zhao, F. Guo, P. Xiao, Evaluation of thermal conductivity of the constituent layers in TRISO particles using Raman spectroscopy, Journal of the European Ceramic Society, 37 (2017) 4457-4465.
[9] E. López-Honorato, C. Chiritescu, P. Xiao, D.G. Cahill, G. Marsh, T.J. Abram, Thermal conductivity mapping of pyrolytic carbon and silicon carbide coatings on simulated fuel particles by time-domain thermoreflectance, Journal of Nuclear Materials, 378 (2008) 35-39.
[10] D. Marchand, D. Rochais, Thermal characterization of high temperature reactor particle layers by photothermal microscopy, Journal of Physics: Conference Series, 214 (2010) 012134.
[11] Y. Wang, D.H. Hurley, E.P. Luther, M.F. Beaux, D.R. Vodnik, R.J. Peterson, B.L. Bennett, I.O. Usov, P. Yuan, X. Wang, M. Khafizov, Characterization of ultralow thermal conductivity in anisotropic pyrolytic carbon coating for thermal management applications, Carbon, 129 (2018) 476-485.

[12] J.D. Stempien, J.D. hunn, R.N. Morris, T.J. Gerczak, P.A. Demkowicz, AGR-2 TRISO Fuel Post-Irradiation Examination Final Report, in, United States, 2021.
[13] J. Hartmann, P. Voigt, M. Reichling, Measuring local thermal conductivity in polycrystalline diamond with a high resolution photothermal microscope, Journal of Applied Physics, 81 (1997) 2966-2972.
[14] B. Li, L. Pottier, J.P. Roger, D. Fournier, K. Watari, K. Hirao, Measuring the anisotropic thermal diffusivity of silicon nitride grains by thermoreflectance microscopy, Journal of the European Ceramic Society, 19 (1999) 1631-1639.
[15] D.H. Hurley, Z. Hua, R.S. Schley, Closeout Phase II Qualification of the Thermal Conductivity Microscope for IMCL, in, United States, 2018.
[16] D.G. Cahill, Analysis of heat flow in layered structures for time-domain thermoreflectance, Review of Scientific Instruments, 75 (2004) 5119-5122.
[17] C. Xing, C. Jensen, Z. Hua, H. Ban, D.H. Hurley, M. Khafizov, J.R. Kennedy, Parametric study of the frequency-domain thermoreflectance technique, Journal of Applied Physics, 112 (2012).
[18] C. Perez, R. Knepper, M.P. Marquez, E.C. Forrest, A.S. Tappan, M. Asheghi, K.E. Goodson, E.O. Ziade, Non-Contact Mass Density and Thermal Conductivity Measurements of Organic Thin Films Using Frequency–Domain Thermoreflectance, Advanced Materials Interfaces, 9 (2022) 2101404.
[19] A.J. Schmidt, R. Cheaito, M. Chiesa, A frequency-domain thermoreflectance method for the characterization of thermal properties, Review of Scientific Instruments, 80 (2009).
[20] K. Hatori, N. Taketoshi, T. Baba, H. Ohta, Thermoreflectance technique to measure thermal effusivity distribution with high spatial resolution, Review of Scientific Instruments, 76 (2005).
[21] T. Favaloro, J.H. Bahk, A. Shakouri, Characterization of the temperature dependence of the thermoreflectance coefficient for conductive thin films, Review of Scientific Instruments, 86 (2015) 024903.
[22] Z. Hua, H. Ban, M. Khafizov, R. Schley, R. Kennedy, D.H. Hurley, Spatially localized measurement of thermal conductivity using a hybrid photothermal technique, Journal of Applied Physics, 111 (2012).
[23] A. Khabari, F.K. Urban, III, P. Griffiths, I. Petrov, Y.-W. Kim, C. Bungay, Nanoparticle beam formation and investigation of gold nanostructured films, Journal of Vacuum Science & Technology B: Microelectronics and Nanometer Structures Processing, Measurement, and Phenomena, 21 (2003) 2313-2318.
[24] D.H. Hurley, R.S. Schley, M. Khafizov, B.L. Wendt, Local measurement of thermal conductivity and diffusivity, Review of Scientific Instruments, 86 (2015).
[25] M. Chase, NIST-JANAF Thermochemical Tables, 4th Edition, in, American Institute of Physics, -1, 1998.
[26] M.F. Ashby, H. Shercliff, D. Cebon, Materials: Engineering, Science, Processing and Design, Elsevier Science, 2013.
[27] C.B. Alcock, V.P. Itkin, M.K. Horrigan, Vapour Pressure Equations for the Metallic Elements: 298–2500K, Canadian Metallurgical Quarterly, 23 (1984) 309-313.
[28] C. Griesbach, T. Gerczak, Y. Zhang, R. Thevamaran, Microstructural heterogeneity of the buffer layer of TRISO nuclear fuel particles, Journal of Nuclear Materials, 574 (2023) 154219.
[29] Y. Wang, Z. Hua, R. Schley, G. Beausoleil Ii, D.H. Hurley, Thermal properties measurement of TRISO particle coatings from room temperature to 900 °C using laser-based thermoreflectance methods, Journal of Nuclear Materials, 565 (2022) 153721.
[30] B. Reznik, K. Norinaga, D. Gerthsen, O. Deutschmann, The effect of cooling rate on hydrogen release from a pyrolytic carbon coating and its resulting morphology, Carbon, 44 (2006) 1330-1334.
[31] A.J. Leide, T.A. Haynes, N. Tzelepi, J. Payne, M. Jordan, S. Knol, J.A. Vreeling, M. Davies, D.T. Goddard, M.J. Pfeifenberger, M. Alfreider, D. Kiener, D. Liu, Measurement of residual stresses in surrogate coated nuclear fuel particles using ring-core focussed ion beam digital image correlation, Nuclear Materials and Energy, 36 (2023) 101470.

[32] J.A. Evans, R.A. Lebensohn, J.R. Harter, K.D. Weaver, Anisotropic temperature-dependent elastic constants and thermal conductivities of TRISO particle coatings, Journal of Nuclear Materials, 565 (2022) 153718.
[33] T.J. Gerczak, J.D. Hunn, R.A. Lowden, T.R. Allen, SiC layer microstructure in AGR-1 and AGR-2 TRISO fuel particles and the influence of its variation on the effective diffusion of key fission products, Journal of Nuclear Materials, 480 (2016) 257-270.
[34] P. Jiang, D. Wang, Z. Xiang, R. Yang, H. Ban, A new spatial-domain thermoreflectance method to measure a broad range of anisotropic in-plane thermal conductivity, International Journal of Heat and Mass Transfer, 191 (2022) 122849.
[35] G.E. Jellison, J.D. Hunn, Optical anisotropy measurements of TRISO nuclear fuel particle cross-sections: The method, Journal of Nuclear Materials, 372 (2008) 36-44.
[36] J.D. Hunn, G.E. Jellison, R.A. Lowden, Increase in pyrolytic carbon optical anisotropy and density during processing of coated particle fuel due to heat treatment, Journal of Nuclear Materials, 374 (2008) 445-452.
[37] K. Jin, S. Mu, K. An, W.D. Porter, G.D. Samolyuk, G.M. Stocks, H. Bei, Thermophysical properties of Ni-containing single-phase concentrated solid solution alloys, Materials & Design, 117 (2017) 185-192.
[38] M. Radovic, E. Lara-Curzio, R.M. Trejo, H. Wang, W.D. Porter, Thermophysical Properties of YSZ and Ni-YSZ as a Function of Temperature and Porosity, in: Advances in Solid Oxide Fuel Cells II: Ceramic Engineering and Science Proceedings, 2006, pp. 79-85.
[39] M. Bechelany, X. Maeder, J. Riesterer, J. Hankache, D. Lerose, S. Christiansen, J. Michler, L. Philippe, Synthesis Mechanisms of Organized Gold Nanoparticles: Influence of Annealing Temperature and Atmosphere, Crystal Growth & Design, 10 (2010) 587-596.
[40] T.G.M. van den Belt, J.H.W. de Wit, The diffusion of platinum and gold in nickel measured by Rutherford backscattering spectrometry, Thin Solid Films, 109 (1983) 1-10.
[41] R.W. Powell, R.P. Tye, M.J. Hickman, The thermal conductivity of nickel, International Journal of Heat and Mass Transfer, 8 (1965) 679-688.
[42] Y. Wang, D.C. Alsmeyer, R.L. McCreery, Raman spectroscopy of carbon materials: structural basis of observed spectra, Chemistry of Materials, 2 (1990) 557-563.
[43] P. Mallet-Ladeira, P. Puech, C. Toulouse, M. Cazayous, N. Ratel-Ramond, P. Weisbecker, G.L. Vignoles, M. Monthioux, A Raman study to obtain crystallite size of carbon materials: A better alternative to the Tuinstra–Koenig law, Carbon, 80 (2014) 629-639.
[44] E. López-Honorato, H. Zhang, R.A. Shatwell, P. Guillermier, D. Manara, P. Xiao, J. Somers, Analysis of the anisotropy, stoichiometry and polytypes in pyrolytic carbon and silicon carbide coatings, Journal of Nuclear Materials, 432 (2013) 334-340.
[45] D.B. Fischbach, KINETICS OF GRAPHITIZATION. I. THE HIGH-TEMPERATURE STRUCTURAL TRANSFORMATION IN PYROLYTIC CARBONS, in, United States, 1966.